ISSN 1674-1056
http://cpb.iphy.ac.cn
http://iopscience.iop.org/cpb
中国物理 B
Chinese Physics
中国物理 Chinese Physics B

Imaging the diffusion pathway of Al^{3+} ion in NASICON-type $(Al_{0.2}Zr_{0.8})_{20/19}Nb(PO_4)_3$ as electrolyte for rechargeable solid-state Al batteries

Jie Wang(王捷), Chun-Wen Sun(孙春文), Yu-Dong Gong(巩玉栋), Huai-Ruo Zhang(张怀若), Jose Antonio Alonso, M T Fernández-Díaz, Zhong-Lin Wang(王中林), John B Goodenough

Citation: Chin. Phys. B . 2018, 27(12): 128201. **doi:** 10.1088/1674-1056/27/12/128201
Journal homepage: http://cpb.iphy.ac.cn; http://iopscience.iop.org/cpb

What follows is a list of articles you may be interested in

Tuning hybrid liquid/solid electrolytes by lowering Li salt concentration for lithium batteries

Wei Yang(杨伟), Qi-Di Wang(王启迪), Yu Lei(雷宇), Zi-Pei Wan(万子裴), Lei Qin(秦磊), Wei Yu(余唯), Ru-Liang Liu(刘如亮), Deng-Yun Zhai(翟登云), Hong Li(李泓), Bao-Hua Li(李宝华), Fei-Yu Kang(康飞宇)

Chin. Phys. B . 2018, 27(6): 068201. **doi:** 10.1088/1674-1056/27/6/068201

Enhanced ionic conductivity in LAGP/LATP composite electrolyte

Shi-Gang Ling(凌仕刚), Jia-Yue Peng(彭佳悦), Qi Yang(杨琪), Ji-Liang Qiu(邱纪亮), Jia-Ze Lu(卢嘉泽), Hong Li(李泓)

Chin. Phys. B . 2018, 27(3): 038201. **doi:** 10.1088/1674-1056/27/3/038201

Pressure-induced structural evolution of apatite-type $La_{9.33}Si_6O_{26}$

Guangchao Yin(尹广超), Hong Yin(殷红), Meiling Sun(孙美玲), Wei Gao(高伟)

Chin. Phys. B . 2018, 27(1): 018202. **doi:** 10.1088/1674-1056/27/1/018202

Forming solid electrolyte interphase *in situ* in an ionic conductingLi$_{1.5}$Al$_{0.5}$Ge$_{1.5}$(PO$_4$)$_3$-polypropylene (PP) basedseparator for Li-ion batteries

Jiao-Yang Wu(吴娇杨), Shi-Gang Ling(凌仕刚), Qi Yang(杨琪), Hong Li(李泓), Xiao-Xiong Xu(许晓雄), Li-Quan Chen(陈立泉)

Chin. Phys. B . 2016, 25(7): 078204. **doi:** 10.1088/1674-1056/25/7/078204

Interfacial transport in lithium-ion conductors

Shaofei Wang(王少飞) and Liquan Chen(陈立泉)

Chin. Phys. B . 2016, 25(1): 018202. **doi:** 10.1088/1674-1056/25/1/018202

Imaging the diffusion pathway of Al^{3+} ion in NASICON-type $(Al_{0.2}Zr_{0.8})_{20/19}Nb(PO_4)_3$ as electrolyte for rechargeable solid-state Al batteries*

Jie Wang(王捷)[1], Chun-Wen Sun(孙春文)[1,6,9,†], Yu-Dong Gong(巩玉栋)[1], Huai-Ruo Zhang(张怀若)[2,3,‡], Jose Antonio Alonso[4,§], María Teresa Fernández-Díaz[5], Zhong-Lin Wang(王中林)[1,6,7,9], and John B Goodenough[8]

[1] *CAS Center for Excellence in Nanoscience, Beijing Institute of Nanoenergy and Nanosystems, Chinese Academy of Sciences (CAS), Beijing* 100083, *China*
[2] *Theiss Research, La Jolla, California* 92037, *USA*
[3] *Material Measurement Laboratory, National Institute of Standards and Technology, Gaithersburg, Maryland* 20899, *USA*
[4] *Instituto de Ciencia de Materiales de Madrid, CSIC, Cantoblanco* 28049 *Madrid, Spain*
[5] *Institut Laue Langevin, BP* 156*X, GrenobleCedex, France*
[6] *School of Nanoscience and Technology, University of Chinese Academy of Sciences, Beijing* 100049, *China*
[7] *School of Material Science and Engineering, Georgia Institute of Technology, Atlanta, GA* 30332-0245, *USA*
[8] *Texas Materials Institute, The University of Texas at Austin, Austin, Texas* 78712, *USA*
[9] *Center on Nanoenergy Research, School of Physical Science and Technology, Guangxi University, Nanning* 530004, *China*

(Received 26 September 2018; revised manuscript received 21 October 2018; published online 10 November 2018)

Among all-solid-state batteries, rechargeable Al-ion batteries have attracted most attention because they involve three-electron-redox reactions with high theoretic specific capacity. However, the solid Al-ion conductor electrolytes are less studied. Here, the microscopic path of Al^{3+}-ion conduction of NASICON-type $(Al_{0.2}Zr_{0.8})_{20/19}Nb(PO_4)_3$ oxide is identified by temperature-dependent neutron powder diffraction and aberration-corrected scanning transmission electron microscopy experiments. $(Al_{0.2}Zr_{0.8})_{20/19}Nb(PO_4)_3$ shows a rhombohedral structure consisting of a framework of $(Zr,Nb)O_6$ octahedra sharing corners with (PO_4) tetrahedra; the Al occupy trigonal antiprisms exhibiting extremely large displacement factors. This suggests a strong displacement of Al ions along the *c* axis of the unit cell as they diffuse across the structure by a vacancy mechanism. Negative thermal expansion behavior is also identified along *a* and *b* axes, due to folding of the framework as temperature increases.

Keywords: aluminum–ion battery, solid electrolyte, diffusion pathway, negative thermal expansion

PACS: 82.33.Pt, 82.45.Gj, 82.45.Xy **DOI:** 10.1088/1674-1056/27/12/128201

1. Introduction

Limitations of the flammable liquid electrolyte of the Li-ion battery have motivated reconsideration of all-solid-state batteries.[1–7] Aluminum (Al) is an abundant, light-weight metal that offers three electrons per atom Al. Therefore, a theoretical specific capacity of 2980 $mAh{\cdot}g^{-1}$ and a volume capacity of 8046 $Ah{\cdot}L^{-1}$ can be achieved.[8,9] Recently, Dai *et al.*[10] reported a rechargeable Al battery with a three-dimensional graphitic-foam cathode that showed high-rate capability and excellent cycling performance up to 7500 cycles at room temperature. However, their cells used an ionic liquid electrolyte, $AlCl_3$/[EMIm]Cl, that is costly and not easy to prepare. Development of an Al battery with a solid electrolyte is plagued by poor Al^{3+} conductivity, σ_{Al}, in the electrolyte. However, Imanaka *et al.* have reported a high σ_{Al} at high temperatures in $(Al_{0.2}Zr_{0.8})_{20/19}Nb(PO_4)_3$.[11]

In this work, we identify the Al diffusion mechanism in $(Al_{0.2}Zr_{0.8})_{20/19}Nb(PO_4)_3$ through high-temperature neutron powder diffraction (NPD) experiments and atomic-resolution scanning transmission electron microscopy (STEM) analyses. Temperature-driven Al displacements indicate that Al^{3+} ions diffuse across the structure by a vacancy mechanism. Furthermore, negative thermal expansion (NTE) behavior was also observed in $(Al_{0.2}Zr_{0.8})_{20/19}Nb(PO_4)_3$ over a wide temperature range by NPD experiments. Importantly, we have demonstrated a rechargeable solid-state Al battery with V_2O_5 nanorods/rGO (reduced graphene oxide) as cathode, a dense $(Al_{0.2}Zr_{0.8})_{20/19}Nb(PO_4)_3$ pellet as electrolyte and Al as anode. Preliminary results show that $(Al_{0.2}Zr_{0.8})_{20/19}Nb(PO_4)_3$ is an electrolyte material for a solid-state Al battery operating at high temperatures. High-temperature batteries are important power sources for aeronautics, astronautics, and military applications.[12–14]

*Project supported by the National Natural Science Foundation of China (Grant Nos. 51672029, 51372271, and 51172275) and the National Key Research and Development Project from the Ministry of Science and Technology, China (Grant No. 2016YFA0202702).

†Corresponding author. E-mail: sunchunwen@binn.cas.cn
‡Corresponding author. E-mail: huairuo.zhang@nist.gov
§Corresponding author. E-mail: ja.alonso@icmm.csic.es

© 2018 Chinese Physical Society and IOP Publishing Ltd

2. Experiment

2.1. Preparation of materials

$(Al_{0.2}Zr_{0.8})_{20/19}Nb(PO_4)_3$ powder was prepared by a solid-state reaction method. The stoichiometric amounts of $Al(OH)_3$, $ZrO(NO_3)_2$, Nb_2O_5, and $(NH_4)_2HPO_4$ (Alfa Aesar Co. Ltd) were mixed for 1 h with an agate mortar and then ball milled for 6 h with ethyl alcohol as a medium. The mixed slurry was dried in an oven overnight at 60 °C to get the precursor and then they were calcined at 600 °C for 6 h. The obtained powder was pelletized under 12 MPa before they were transferred to a muffle furnace and heated at 1025 °C for 14 h in air with a heating/cooling rate of 5 °C/min. The pellets were then pulverized, ground and pelletized again before heated to 1225 °C, and then 1275 °C and 1325 °C for 14 h, respectively.

The V_2O_5 nanorods/rGO composite cathode was prepared according to the literature.[14]

2.2. Structural Characterization

X-ray diffraction (XRD) was performed with a Bruker-AXS D8 diffractometer (40 kV, 30 mA) with Cu Kα radiation ($\lambda = 1.5418$ Å). Neutron powder diffraction (NPD) data were collected in the D2B diffractometer at the Institut Laue-Langevin, Grenoble with $\lambda = 1.594$ Å. For the RT acquisition, about 3 g of sample was contained in a vanadium can. For the high-temperature acquisitions, the sample holder was placed in the isothermal zone of a furnace with a vanadium resistor operating under vacuum ($P_{O_2} \approx 10^{-6}$ Torr, 1 Torr = 1.33322×10^2 Pa). The measurements were carried out at 200, 400, 600, and 800 °C, respectively. The collection time was 2 h per pattern. The diffraction data were all analysed by the Rietveld method with the FULLPROF program[15] and the use of its internal tables for scattering lengths. The line shape of the diffraction peaks was generated by a pseudo-Voigt function. The irregular background coming from the furnace was extrapolated from points devoid of reflections. In the final run, the following parameters were refined: background points, zero shift, half-width, pseudo-Voigt and asymmetry parameters for the peak shape, scale factor and unit-cell parameters. Two regions with peaks coming from the experimental environment were excluded from the refinement. Isotropic thermal factors for all the metal atoms and anisotropic for aluminium atoms were also refined for the NPD data. The coherent scattering lengths for Al, Nb, Zr, P, and O were, 3.449, 7.054, 7.160, 5.130, and 5.803 fm (1 fm = 10^{-15} m), respectively.

TEM samples were prepared from $(Al_{0.2}Zr_{0.8})_{20/19}Nb(PO_4)_3$ pellets using a Gatan precision ion polishing system (PIPS II). A double aberration-corrected microscope JEM-Z3100F-R005 STEM/TEM operated at 300 keV was employed to do EDPs, HRTEM and STEM analyses. HRTEM images were collected with a negative spherical aberration (Cs) coefficient ~ -30 μm and slight over focus to obtain bright atomic images. An image simulation software JEMS was used to simulate HRTEM images with multislice computation method. The crystal structural model proposed by neutron diffraction analysis at 25 °C was used for the HRTEM image simulation. Atomic resolution HAADF-STEM images were collected with a probe convergence semi-angle of 24 mrad, and HAADF detector semi-angular collection range 42 mrad–240 mrad.

2.3. Assembling Al-ion cells

Electrochemical performance testing was performed with swagelok cells. The cells consisting of the V_2O_5 nanorods/graphene as cathode, aluminum as anode and the prepared dense $(Al_{0.2}Zr_{0.8})_{20/19}Nb(PO_4)_3$ solid pellet ($\sim$ 300 μm in thickness, 13 mm in diameter) as electrolyte were assembled in an Ar-filled glove box. Typically, for anode preparation, aluminum was deposited on one side of the dense electrolyte pellet by a magnetron sputtering technique (Kurt J Lesker PVD75 Proline, USA) and subsequently sputtered Au coating as the current collector by a sputtering machine (Cressington 108 auto, UK).[16] For improving the ion diffusion issue between the cathode/electrolyte interface, a small amount of the molten-salts electrolyte consisting of sodium chloride (99.99%) and aluminium chloride (99.9%) (1:1.63 in mole ratio) was introduced, as reported in the literature.[17,18] The cathode area is 0.785 cm^2 and the active mass of the cathode is about 2 $mg{\cdot}cm^{-2}$. Galvanostatic discharge/charge test was carried out in the voltage range of 0.01 V–2.0 V at a current density of 2 $mA{\cdot}g^{-1}$ at 120 °C and 150 °C on a LAND battery testing system, respectively.

2.4. Electrochemical measurement

For impedance spectra measurements, the obtained powder was pressed at 15 MPa into pellets. The pellets are 13 mm in diameter. The thickness of the pellets is about 1 mm. The pellets were then coated with platinum paste on both sides. AC impedance spectroscopy was measured with an electrochemical workstation (Zahner IM6E) over a frequency range from 100 mHz to 1 MHz. An applied voltage was fixed at 10 mV. All measurements were done in temperature range of 300 °C to 600 °C.

3. Results and discussion

$(Al_{0.2}Zr_{0.8})_{20/19}Nb(PO_4)_3$ was prepared by solid-state reaction. The phase and crystal structure of the product were examined by powder x-ray diffraction (XRD); the pattern is shown in Supplementary Material, Fig. S1. All of the peaks of the well-crystallized structure correspond to the rhombohedral NASICON phase isostructural to $NaZr_2(PO_4)_3$.[19,20] The octahedrally coordinated Zr^{4+} are partially replaced by Nb^{5+},

which reduce the volume of the unit cell sufficiently to accommodate the small Al^{3+} (0.535 Å in octahedral coordination) in the interstitial space of the M(II) site of the structure.[21] In $NaZr_2(PO_4)_3$, the Na^+-ions occupy the interstitial M(I) sites, and in $(Al_{0.2}Zr_{0.8})_{20/19}Nb(PO_4)_3$, the M(I) sites are occupied by Nb and/or Zr. Our original strategy was to also increase the oxygen bonding of the framework to reduce the strength if the Al^{3+} is bonded to the framework.[11]

Electron-diffraction pattern (EDP) and aberration-corrected high-resolution transmission electron microscopy (HRTEM) taken at 25 °C were also performed to characterize the crystal structure. All of the EDPs and HRTEM images can also be well-indexed with a NASICON-type model (Supplementary Material, Fig. S2, Table S1). Atomic-resolution high-angle annular dark field (HAADF) imaging was performed with an aberration-corrected scanning transmission electron microscopy (STEM) to observe the Al^{3+} distribution. Figure 1(a) shows a Z-contrast (Z: atomic number) HAADF image of $(Al_{0.2}Zr_{0.8})_{20/19}Nb(PO_4)_3$ taken along the [010] zone-axis. Atomic columns of Zr/Nb, P and Al in the HAADF image can be identified by the intensity of projected atomic columns; they correspond to a NASICON structural model of a unit cell viewed along the [010] zone-axis, as shown in the inset. Al^{3+}-ion columns are shown by the yellow arrows; Al^{3+}-ionic channels can be identified in the {10-2} crystallographic planes. Figure 1(b) shows the intensity profile of the Al^{3+} ion columns along a dash–dot line AB in Fig 1(a). The variation of the intensity of the Al^{3+}-site suggests a random distribution of Al^{3+} and vacancies, which promotes transportation of Al^{3+} in the ionic channel.

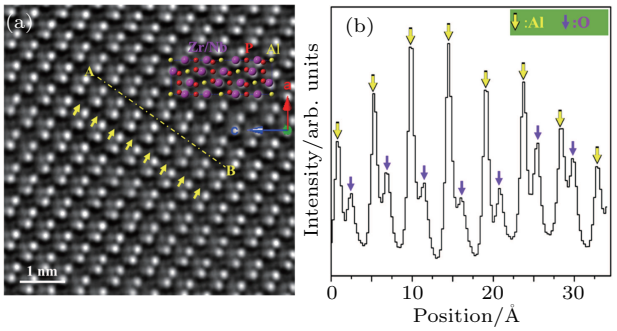


Fig. 1. (color online) Room temperature STEM characterizations of $(Al_{0.2}Zr_{0.8})_{20/19}Nb(PO_4)_3$. (a) Atomic resolution HAADF image overlapped with a structural model of a unit cell viewed along [010] zone-axis. The magenta, red and yellow spheres represent Nb/Zr, P, and Al site respectively. Oxygen was omitted for clarity. Yellow arrows illustrate the Al^{3+} ion columns. (b) Intensity profile measured from the dash–dot line AB in panel (a), yellow arrows illustrating the position of Al^{3+}-site. The weak peaks shown by the magenta arrows come from the O^{2-} ion columns along the dash–dot line AB.

An investigation of the crystal structure by NPD was performed to determine structural details, since neutrons allow us to explore a much wider range of the reciprocal space and the lack of form factor permits the precise determination of the anisotropic displacement factors. The neutron pattern confirms the rhombohedral symmetry with $a = b = 8.7509(2)$ Å and $c = 22.4368(7)$ Å in the hexagonal setting at 25 °C; the structure was defined in the R-3c space group (No. 167) with Al located at 6b Wyckoff site $(0,0,0)$; Nb and Zr distributed at random at 12c $(0,0,z)$ site; P at 18e $(x, 0, 1/4)$ positions and the two types of oxygen O at 36f (x,y,z) sites. The Nb and Zr occupancy factors were defined according to the nominal stoichiometry; the Al occupancy factor was also fixed to the nominal composition since it was found to be strongly correlated with its thermal displacement factors. The final structural parameters and agreement factors are gathered in Supplementary Material, Table S1.

Conductivity measurements, as described later, demonstrate that $(Al_{0.2}Zr_{0.8})_{20/19}Nb(PO_4)_3$ is an exceptionally good solid-state conductor for Al^{3+} ions. A temperature-dependent NPD study appears to be critical to understand the crystal structure evolution with the functional temperatures of this material. NPD diagrams collected at 200, 400, 600, and 800 °C with $\lambda = 1.594$ Å show the same crystal symmetry but dramatic changes in the magnitude and anisotropy of the displacement parameters. All the peaks can be indexed in the rhombohedral R-3c unit cell, which demonstrates the structure is stable at these working conditions. The access to a wide region of the reciprocal space allowed us a successful refinement of the anisotropic displacement factors of the aluminum atoms. The good agreement between observed and calculated profiles is displayed in the patterns tested at 25 °C and 800 °C, respectively (Supplementary Material, Figs. S3(a) and S3(b)). Figures 2(a) and 2(b) illustrate the evolution of the rhombohedral crystal structure (hexagonal setting) displaying a remarkable anisotropy in the cigar-shaped (prolate) displacement ellipsoids for aluminum. Table S1 contains the main structural parameters of the crystal structures at 200, 400, 600, and 800 °C, and Table S2 contains the main bond distances and angles. Figures 2(c)–2(e) display the thermal variation of the unit-cell parameters and volume, figure 2(f) shows the evolution of the B_{eq} thermal displacement for Al across the measured temperature range.

It is remarkable that whereas the c parameter expands upon heating, the a parameter contracts in all the studied temperature range (25 °C–800 °C), yielding an overall, anisotropic volume contraction as temperature is increased. The thermal expansion coefficient based upon the volume variation may be defined as $\alpha_V = (V_T - V_0)/V_0(T - T_0)$, giving $\alpha_V = -4.49 \times 10^{-6}$ K^{-1}. If we estimate the contraction experienced along the a or b direction, according to $\alpha_l = (l_T - l_0)/l_0(T - T_0)$, we obtain $\alpha_a = -3.92 \times 10^{-6}$ K^{-1}. The expansion along c is $\alpha_c = 3.37 \times 10^{-6}$ K^{-1}. This anisotropic thermal expansion has been observed before in other NASICON-type structures.[22,23] The origin of the observed NTE has been previously described as a folding of the structure on warming up. The microscopic origin of the NTE is identified by our NPD data.

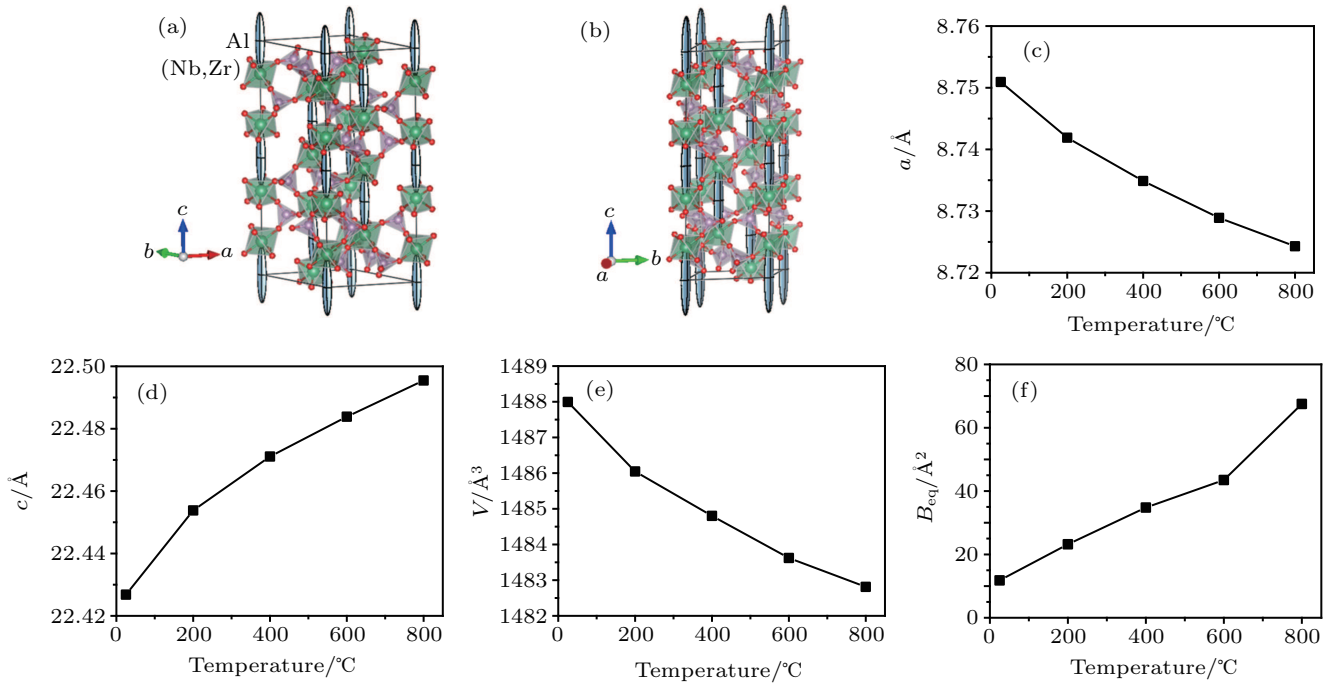


Fig. 2. (color online) (a) and (b) Crystal structure of $(Al_{0.2}Zr_{0.8})_{20/19}Nb(PO_4)_3$ consisting of a framework of $(Nb,Zr)O_6$ octahedra sharing corners with PO_4 tetrahedra. The strongly anisotropic thermal displacements of the Al^{3+} ions with the ellipsoids directed along the [001] directions are enhanced at (a) 200 °C, and (b) 800 °C. Thermal variation of [panels (c) and (d)] unit-cell parameters and (e) volume, and (f) thermal displacement (B_{eq}) of Al.

The magnitude of the thermal displacement increases monotonically with temperature, as is shown in Table S1 and Fig. S3. The anisotropy of the Al thermal ellipsoids has the largest thermal displacement along the *c* axis. At 800 °C, the root mean square (r.m.s.) displacements of Al are 1.56 Å along the [001] direction, and 0.1 Å and 0.01 Å perpendicular to it, in a flattened and extraordinarily elongated prolate configuration (Fig. S3). As discussed later, this configuration shows a strong displacement of the Al atoms, even penetrating into the adjacent $(Nb,Zr)O_6$ octahedra that contain some vacancies at 800 °C for the nominal composition $(Al_{0.2}Zr_{0.8})_{20/19}Nb(PO_4)_3$, implying that 8% of the octahedral M(I) positions are empty. Diffusion by a vacancy diffusion mechanism is possible because only 41% of the 6*b* positions are occupied by Al atoms. This result is consistent with the HRTEM results. Given the rombohedral symmetry, a largely anisotropic Al diffusion would be expected for this compound, mainly along the *c* axis.

The feasibility of a dense $(Al_{0.2}Zr_{0.8})_{20/19}Nb(PO_4)_3$ pellet as a solid electrolyte material was investigated by impedance spectra measurements. The cross sectional SEM images of the prepared $(Al_{0.2}Zr_{0.8})_{20/19}Nb(PO_4)_3$ pellet are shown in Fig. S4. Swagelok cells were prepared with V_2O_5 nanorods/graphene as cathode,[24] aluminum as anode and the dense $(Al_{0.2}Zr_{0.8})_{20/19}Nb(PO_4)_3$ solid pellet (∼ 300 μm in thickness) as electrolyte. Figure 3(a) shows the schematic diagram of the swagelok cell used for electrochemical tests. Figure 3(b) illustrates the preparation process of the anode. The temperature dependence of the Al^{3+} conductivity of $(Al_{0.2}Zr_{0.8})_{20/19}Nb(PO_4)_3$ is shown in Fig. 3(c). By fitting the slope of the Arrhenius plots, the activation energy (E_a) of the electrolyte was determined using the Arrhenius equation:

$$\sigma = \sigma_0 \exp\left(-\frac{E_a}{kT}\right). \quad (1)$$

The activation energy E_a calculated from the slope is 3.1 eV. Figure 3(d) shows the initial discharge–charge curves of a cell from 0.01 V to 2.0 V versus Al^{3+}/Al at a current density of 2 mA·g^{-1}. The initial discharge specific capacity reaches 7.5 mAh·g^{-1} at 120 °C while the charge specific capacity is 6.5 mAh·g^{-1}. As the temperature is increased to 150 °C, a capacity value of ∼ 10 mAh·g^{-1} is achieved. The voltages of discharge/charge processes are similar to those reported in the literatures.[16]

The $(Al_{0.2}Zr_{0.8})_{20/19}Nb(PO_4)_3$ crystal structure is a three-dimensional (3D) network containing vertex-linked $(Nb,Zr)O_6$ octahedra and PO_4 tetrahedra, with the Al-ions partially occupying interstitial trigonal antiprism spaced at intervals along the *c* axis. There is only one crystallographically distinct Al site. Figure 4 displays the coordination of the Al site, the size of which is basically determined by the distance between O_2 atoms along the *c* direction. The NPD results clearly show that the rhombohedral structure, defined in the space group *R*-3*c*, is stable across the temperature range 25 °C to 800 °C because no superstructure reflections (Fig. S3(a)) justify a departure of this symmetry to describe the crystal structure.

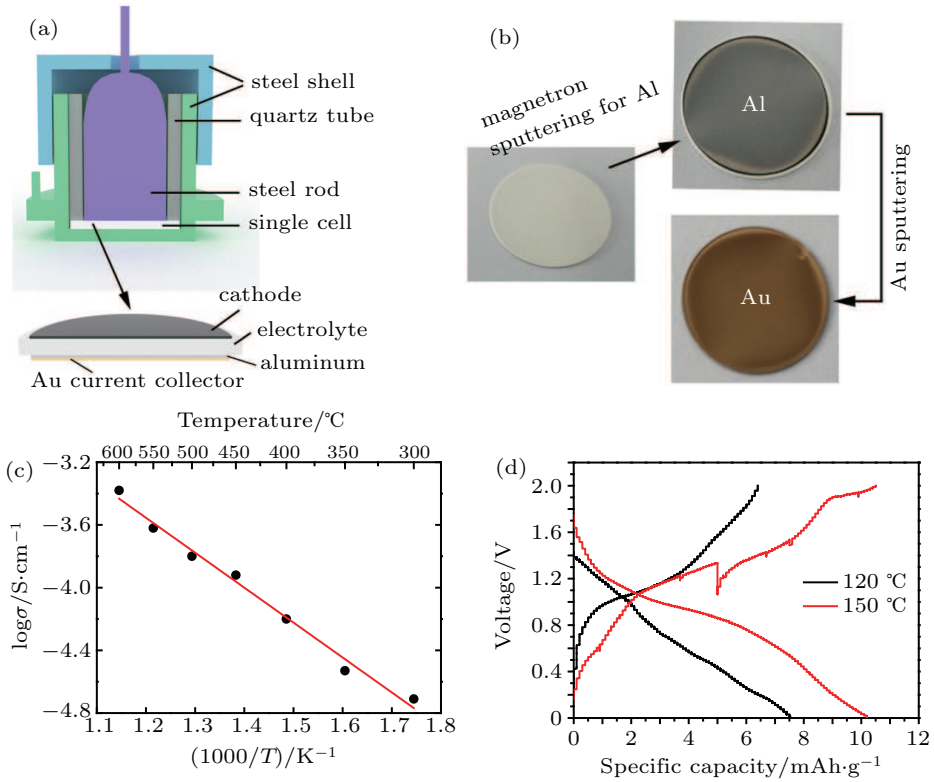


Fig. 3. (color online) (a) Schematic diagram of the swagelok cell used for electrochemical tests. (b) The preparation process of Al anode. (c) Temperature dependence of the Al^{3+} ion conductivity of $(Al_{0.2}Zr_{0.8})_{20/19}Nb(PO_4)_3$. (d) Initial discharge–charge profiles of the solid-state V_2O_5 nanorods/rGO|Al battery at a current density of 2 mA·g^{-1} at 120 °C and 150 °C, respectively.

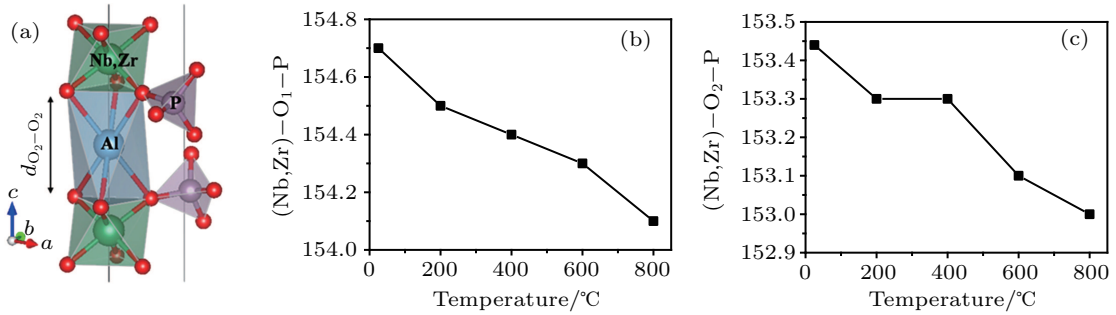


Fig. 4. (color online) (a) Close-up of the crystal structure highlighting the Al coordination polyhedra, defined as a trigonal antiprism, where the O_2–O_2 distances determine the size of the polyhedron and the length of the *c* unit-cell axis; (b) and (c) thermal variation of the (Nb,Zr)–O–P angles, determining the tilting angle between octahedral and tetrahedral units in the framework of $(Al_{0.2}Zr_{0.8})_{20/19}Nb(PO_4)_3$.

The thermal expansion of the *c* axis observed in this temperature range may be explained by the expansion of the *c*-axis O_2–O_2 separation of the Al site. This governs the 'size' of the trigonal prismatic site along the *c* axis. Between 25 °C and 800 °C the O_2–O_2 distances along the *c* axis ($d_{O_2-O_2}$ in Fig. 4(a)) increase from 2.07 Å to 2.08 Å, accounting for the overall expansivity α_c. Regarding the contraction of the *a* parameter, figures 4(b) and 4(c) demonstrate that there is a folding of the crystal structure in such a way that (Nb,Zr)–O–P angles become smaller upon heating, which is ascribed to transverse vibration modes called "guitar string" vibrations that tend to bend the chemical bonds and lead to NTE.[23] NTE behavior was observed in $(Al_{0.2}Zr_{0.8})_{20/19}Nb(PO_4)_3$ over a wide temperature range.

This NTE behavior is a general trend in many framework works containing octahedral and tetrahedral units, such as ZrW_2O_8,[24,25] $ZrMo_2O_8$,[26] and other NASICON-type structures including the related Al-free $NbZr(PO_4)_3$ with ($\alpha_l = 2.3\times10^6$)[27] and $(HfSc)_{0.83}W_{2.25}P_{0.83}O_{12\delta}$.[28] This behavior is a consequence of the structural constraint of atomic bridging motifs.[26] The ability to bend these linkages at the O atoms means that the dominant thermal response is associated with flexing bonds rather than stretching them, and the geometrical flexibility explains why the crystallites deform readily in response to thermal and/or mechanical stress in NTE materials.

The high Al^{3+} conductivity is primarily linked to the weak chemical bonds established between Al and O_2 in an oversized cage exhibiting Al–O_2 distances in the 2.64 Å–2.65 Å range. The ionic radii sums for Al^{3+} (i.r.(VI) = 0.535 Å) (16) and O^{2-} (i.r.(IV) = 1.38 Å) is just 1.915 Å, meaning

that Al ions are rattling in the cages, as is visualized by the large displacement factors observed even at room temperature. It is noteworthy that the orientation of the anisotropic thermal displacements is along the axial directions of the trigonal antiprism; *i.e.*, approximately along the bonding direction within the octahedra. This arrangement of the thermal ellipsoids is not the one usually found in oxides; normally the thermal vibrations are perpendicular to the chemical bonds, displaying oblate spheroids. Taking the cubic perovskite $Ba_{0.87}K_{0.13}BiO_3$[27] as an example, the oblate vibrations lock the oxygen atoms at mid-bismuth positions with enhanced vibrations perpendicular to the Bi–Bi distance. A prolate ellipsoid for the oxygen anisotropic thermal displacement parameters indicates a softening of "breathing" modes at the bismuth atoms. In the present $(Al_{0.2}Zr_{0.8})_{20/19}Nb(PO_4)_3$ phosphate, the prolate thermal ellipsoids of the Al^{3+} ions are oriented along the chemical bonds and are clearly correlated with the Al diffusivity.

4. Conclusion

In the present investigations, the NASICON-type oxide $(Al_{0.2}Zr_{0.8})_{20/19}Nb(PO_4)_3$ is a good solid-state conductor for Al^{3+} ions. Temperature-dependent neutron powder diffraction (NPD) and aberration-corrected scanning transmission electron microscopy (STEM) experiments identify a strong displacement of Al ions along the *c* axis of the unit cell as they diffuse across the structure by a vacancy mechanism. The Al^{3+} conductivity and NTE of the $(Al_{0.2}Zr_{0.8})_{20/19}Nb(PO_4)_3$ may be applicable in wide applications, such as solid-state Al batteries and precision optical devices used on satellites.[29]

Acknowledgment

One of the authors (Zhang H) acknowledges support from the U.S. Department of Commerce, National Institute of Standards and Technology under the financial assistance award 70NANB17H249. Alonso J A thanks the Spanish MINECO for granting the project MAT2017-84496-R, Spain, and ILL for making all facilities available for the neutron diffraction experiments.

References

[1] Kamaya N, Homma K, Yamakawa Y, Hirayama M, Kanno R, Yonemura M, Kamiyama T, Kato Y, Hama S, Kawamoto K and Mitsui A 2011 *Nat. Mater.* **10** 682
[2] Quartarone E and Mustarelli P 2011 *Chem. Soc. Rev.* **40** 2525
[3] Sun C W, Liu J, Gong Y, Wilkinson D P and Zhang J J 2017 *Nano Energy* **33** 363
[4] Bates J B, Dudney N J, Neudecker B, Ueda A and Evans C D 2000 *Solid State Ionics* **135** 33
[5] Hou H D, Xu Q K, Pang Y K, Li L, Wang J L, Zhang C and Sun C W 2017 *Adv. Sci.* **4** 1700072
[6] Shi M L, Liu L, Tian F H, Wang P F, Li J J and Ma L 2017 *Acta Phys. Sin.* **66** 208201 (in Chinese)
[7] Ling S G, Peng J Y, Yang Q, Qiu J L, Lu J Z and Li H 2018 *Chin. Phys. B* **27** 038201
[8] Elia G A, Marquardt K, Hoeppner K, Fantini S, Lin R Y, Knipping E, Peters W, Drillet J F, Passerini S and Hahn R 2016 *Adv. Mater.* **28** 7564
[9] Ambroz F, Macdonald T J and Nann T 2017 *Adv. Energy Mater.* **7** 1602093
[10] Lin M C, Gong M, Lu B, Wu Y, Wang D Y, Guan M, Angell M, Chen C, Yang J, Hwang B J and Dai H 2015 *Nature* **520** 324
[11] Imanaka N, Hasegawa Y, Yamaguchi M, Itaya M, Tamura S and Adachi G 2002 *Chem. Mater.* **14** 4481
[12] Robertson A D, West A R and Ritchie A G 1997 *Solid State Ionics* **104** 1
[13] Heriksen G L and Vissers D R 1994 *J. Power Sources* **51** 115
[14] Zhang Y, Lai J Y, Gong Y D, Hu Y M, Liu J, Sun C W and Wang Z L 2016 *ACS Appl. Mater. Interfaces* **8** 34309
[15] Rodríguez-Carvajal J 1993 *Physica B* **192** 55
[16] Chiku M, Takeda H, Matsumura S, Higuchi E and Inoue H 2015 *ACS Appl. Mater. Interfaces* **7** 24385
[17] Song Y, Jiao S, Tu J, Liu Y, Jiao H, Mao X, Guo Z and Fray D J 2017 *J. Mater. Chem. A* **5** 1282
[18] Wang H, Bai Y, Chen S, Luo X, Wu C, Wu F, Lu J and Amine K 2015 *ACS Appl. Mater. Interfaces* **7** 80
[19] Hagman L O and Kierkegaard P 1968 *Acta Chem-. Scand.* **22** 1822
[20] Bennouna L, Arsalane S, Brochu R, Lee M R, Chassaing J and Quarton M 1995 *J. Solid State Chem.* **114** 224
[21] Shannon R D 1976 *Acta Crystallogr. Sect. A* **32** 751
[22] Evans J S O 1999 *J. Chem. Soc. Dalton Trans.* **19** 3317
[23] Taylor D 1991 *Br. Ceram. Trans.* **90** 64
[24] Mary T A, Evans J S O, Vogt T and Sleight A W 1996 *Science* **272** 90
[25] Chen J, Deng J X, Yu R B, Sun C, Hu P H and Xing X R 2010 *Physics* **39** 691 (in Chinese)
[26] Lind C, Wilkinson A P, Hu Z, Short S and Jorgensen J D 1998 *Chem. Mater.* **10** 2335
[27] Wignacourt J P, Swinnea J S, Steinfink H and Goodenough J B 1988 *Appl. Phys. Lett.* **53** 1753
[28] Liang Y, Cheng Y G, Ge X H, Yuan B H, Guo J, Sun Q and Liang E J 2017 *Chin. Phys. B* **26** 106501
[29] Goodwin A L, Calleja M, Conterio M J, Dove M T, Evans J S O, Keen D A, Peters L and Tucker M G 2008 *Science* **319** 794